JCB Journal of Cell Biology

REPORT

Active and inactive β1 integrins segregate into distinct nanoclusters in focal adhesions

Matthias Spiess[1]*, Pablo Hernandez-Varas[1,2]*, Anna Oddone[3], Helene Olofsson[1], Hans Blom[4], Dominic Waithe[2], John G. Lock[1], Melike Lakadamyali[3], and Staffan Strömblad[1]

Integrins are the core constituents of cell–matrix adhesion complexes such as focal adhesions (FAs) and play key roles in physiology and disease. Integrins fluctuate between active and inactive conformations, yet whether the activity state influences the spatial organization of integrins within FAs has remained unclear. In this study, we address this question and also ask whether integrin activity may be regulated either independently for each integrin molecule or through locally coordinated mechanisms. We used two distinct superresolution microscopy techniques, stochastic optical reconstruction microscopy (STORM) and stimulated emission depletion microscopy (STED), to visualize active versus inactive β1 integrins. We first reveal a spatial hierarchy of integrin organization with integrin molecules arranged in nanoclusters, which align to form linear substructures that in turn build FAs. Remarkably, within FAs, active and inactive β1 integrins segregate into distinct nanoclusters, with active integrin nanoclusters being more organized. This unexpected segregation indicates synchronization of integrin activities within nanoclusters, implying the existence of a coordinate mechanism of integrin activity regulation.

Introduction

Formation of integrin-based cell–matrix adhesion complexes such as focal adhesions (FAs) mediates cell–ECM attachment while also enabling bidirectional signaling across the plasma membrane (Lock et al., 2008; Geiger and Yamada, 2011; Han and de Rooij, 2016). Integrin-mediated signaling governs key cellular processes and broadly influences physiology and pathology (Hynes and Naba, 2012). Human β1 integrins adhere to collagens, laminins, fibronectin, and other ECM glycoproteins (Hynes, 2002). ECM adhesion is achieved through specific ligand-binding regions in the integrin extracellular domain, whereas a short cytoplasmic tail mediates intracellular interactions. Importantly, integrin extracellular domains fluctuate between bent and extended conformations whose equilibrium can be modulated by intra- and extracellular cues (Campbell and Humphries, 2011). Different, yet largely overlapping definitions of integrin activity states exist depending on whether the readout is signaling activity, ligand binding, or integrin conformation. One definition holds that integrin activation involves conversion from a bent, closed conformation to a fully extended, open conformation. These conformations are generally considered to reflect inactive and active states, respectively, with intermediate states also being possible (Moser et al., 2009; Su et al., 2016). Integrin activity can also be defined by ECM–ligand binding status, with bound versus nonbound states generally overlapping with extended/open/active versus bent/closed/inactive conformations, respectively. Although all integrin conformations may be found on the cell surface even in the absence of an ECM ligand, almost all resting (unbound) α5β1 integrins are found in the bent/closed/inactive state because this conformation is energetically favorable without additional inputs (Li et al., 2017). However, the extended/open conformation is stabilized in the presence of ECM ligands (Hantgan et al., 2001) because of its high affinity for these targets (Zhu et al., 2013), explaining the larger proportion of extended integrins found in attached cells. Active integrin populations may also be enhanced by intracellular cytoskeletal engagement (Zhu et al., 2008) through scaffold proteins such as talin, kindlin, and vinculin, linking integrins to F-actin (Horton et al., 2015), whereas ICAP and SHARPIN can shift integrins toward an inactive conformation (Bouvard et al., 2013).

[1]Department of Biosciences and Nutrition, Karolinska Institutet, Huddinge, Sweden; [2]Wolfson Imaging Centre, Weatherall Institute of Molecular Medicine, University of Oxford, Oxford, England, UK; [3]Institut de Ciències Fotòniques, Barcelona, Spain; [4]Science for Life Laboratory, Royal Institute of Technology, Solna, Sweden.

*M. Spiess and P. Hernandez-Varas contributed equally to this paper; Correspondence to Staffan Strömblad: staffan.stromblad@ki.se; Anna Oddone's present address is Centre for Genomic Regulation, The Barcelona Institute of Science and Technology, Barcelona, Spain; John G. Lock's present address is School of Medical Sciences, University of New South Wales, Sydney, Australia; Melike Lakadamyali's present address is Dept. of Physiology, Perelman School of Medicine, University of Pennsylvania, Philadelphia, PA.

https://doi.org/10.1083/jcb.201707075

Table 1. **Anti–β1 integrin mAbs**

Clone	Species	Epitope	Conformational specificity	Function	Classification	References
K20	Mouse	EGF-like repeats	Pan	-	Total	Amiot et al. (1986); Takada and Puzon (1993)
9EG7	Rat	EGF-like repeats	Extended; LIBS[a]	Activating	Active	Lenter et al. (1993); Bazzoni et al. (1995); Su et al. (2016)
12G10	Mouse	βA domain	Open headpiece; LIBS	Activating	Active	Mould et al. (1995, 1996Su et al. (2016)
Huts-4	Mouse	Hybrid domain	Open headpiece; LIBS	Activating	Active	Luque et al. (1996); Su et al. (2016)
mAb13	Rat	βA domain	Closed headpiece; LABS	Inhibitory	Inactive	Akiyama et al. (1989); Mould et al. (1996); Su et al. (2016)
AIIB2	Rat	βA domain	LABS	Inhibitory	Inactive	Fig. S1; Werb et al. (1989); Takada and Puzon (1993); Park et al. (2008)

We defined β1 integrin subpopulations labeled by different mAbs as total, active, and inactive as described in Materials and methods. All mAbs defined as active in this study label the same subpopulation as seen by a maximal colocalization (Fig. 3).
[a]Ligand-induced binding site.

Importantly, it remains unclear to what extent integrin activity regulation occurs discretely at the level of individual integrin molecules or whether coordinating mechanisms exist to locally synchronize integrin activity states, as has been shown for regulation of integrin clustering at the scale of entire FAs (Paszek et al., 2014). This raises broader questions about the FA nanoscale spatial architecture. Until recently, the diffraction-limited resolution of light microscopy (~220 nm) hampered detailed observation of FA nanostructure. Superresolution microscopy techniques have overcome this limit, each combining distinct advantages and limitations. For example, stochastic optical reconstruction microscopy (STORM) achieves superresolution imaging by promoting stochastic blinking of individual fluorescent molecules, enabling high-precision molecular localization (Rust et al., 2006). In contrast, stimulated emission depletion (STED) microscopy utilizes shaped, high-power depletion laser lines to spatially constrain fluorophore emission, producing superresolution images (Klar and Hell, 1999). Because STORM and STED are based on distinct principles and image analysis approaches, the combined use of these techniques can provide independent data on nanoscale organization, solving complex biological questions with strengthened confidence (Tam and Merino, 2015).

Recent superresolution imaging has challenged the view of FAs as homogeneous micron-scale protein assemblies, and more sophisticated models are emerging (Shibata et al., 2012). For example, cryoelectron tomography delineated actin-linked clusters within FAs (Patla et al., 2010); photoactivated localization microscopy of FA scaffold proteins vinculin and paxillin suggested the presence of FA nanoclusters (Shroff et al., 2007); structured illumination microscopy revealed paxillin arrangements in linear FA substructures (Hu et al., 2015); three molecular sublayers were identified along the z axis of FAs using interferometric photoactivated localization microscopy (iPALM; Kanchanawong et al., 2010); and single-molecule tracking revealed dynamic integrin reorganization within adhesion substructures (Diez-Ahedo et al., 2009) besides identifying distinct diffusive behaviors for different integrin subunits within FAs (Rossier et al., 2012).

Despite these advances, the fundamental question of how integrins are organized within FAs remains largely unsolved. We show in this study that both active and inactive β1 integrin populations are arranged in nanoclusters within FAs. Surprisingly, these populations are largely segregated such that nanoclusters tend to be enriched in either active or inactive integrin β1. This suggests for the first time that integrin activity is not only regulated at the level of individual molecules but also undergoes a form of collective or coordinate regulation at the level of nanoclusters.

Results and discussion

β1 integrin organization within FAs

Anti-β1 (total β1) integrin mAb K20 (Table 1)–labeled Hs578T cells attached to fibronectin were imaged in both confocal and STED mode (Fig. 1 A). With the increased resolution of STED, the intraadhesion β1 integrin organization became visible as distinct intensity peaks (Fig. 1, A and B). Intensity line profiles comparing an identical adhesion in confocal and STED modes confirmed the presence of discrete intensity peaks in STED images (Fig. 1 B). Intensity peak analysis was automated with Imaris to cover the entire STED dataset, revealing the nanoorganization of β1 integrins within FAs as exemplified in Fig. 1 C. Complementarily, STORM revealed β1 integrin enrichment in small intraadhesion clusters, not visible in diffraction-limited total internal reflection fluorescence (TIRF) images (Fig. 1 D). Density-based spatial clustering analysis with noise (DBSCAN; Ester et al., 1996; Nan et al., 2013) identified these localization clusters within FAs (Fig. 1 D). The detection of intensity peaks in STED and localization clusters in STORM unveils the underlying suborganization of β1 integrins within FAs as has been suggested for other FA components (Changede and Sheetz, 2017). We term these structures nanoclusters. We did not observe enrichment of integrin nanoclusters in any particular region within FAs.

Active and inactive β1 integrin subpopulations form distinct nanocluster patterns

We then asked how integrin activity states may relate to nanocluster organization. Importantly, variability in β1 integrin activation state is reflected by distinct integrin conformations. We

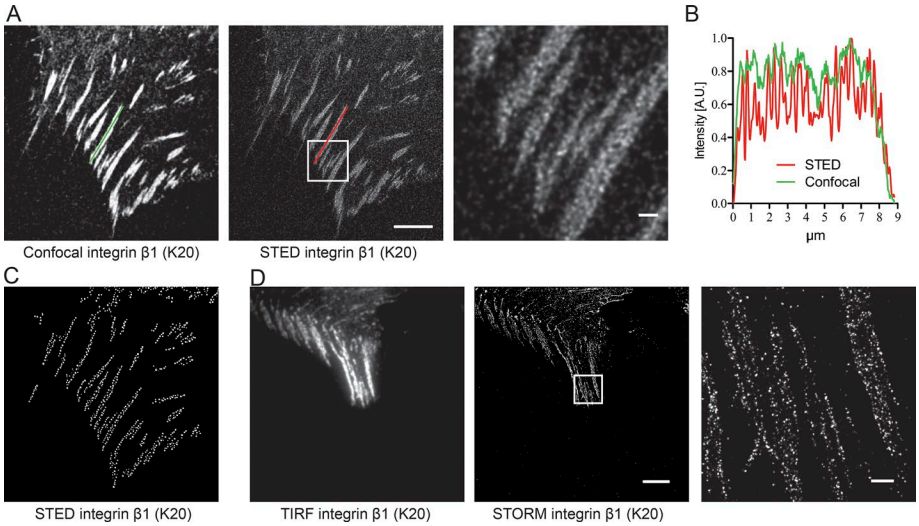

Figure 1. **Nanoorganization of β1 integrins within FAs. (A)** Representative images of an Hs578T cell labeled by anti–total β1 integrin mAb K20 (OG488) acquired by confocal microscopy (left) and STED (middle). The white box in the middle panel is zoomed in the right inset. **(B)** Representative intensity profiles along an individual adhesion (green/red lines in A; $n = 10$, one profile per image) reveal distinct intensity peaks by STED (red) but not by confocal microscopy (green). **(C)** Spatial distribution of identified intensity peaks within adhesions in the STED image from A. **(D)** Representative image of an Hs578T cell labeled with anti–β1 integrin mAb K20 (Alexa Fluor 405 through Alexa Fluor 647) acquired by TIRF (left) and STORM (middle). The white box is zoomed in on the right and shows clusters identified by DBSCAN. Bars: (main images) 5 μm; (insets) 500 nm.

took advantage of well-characterized anti–β1 integrin mAbs with functional and conformational specificity (Table 1; Byron et al., 2009; Campbell and Humphries, 2011). As described in Materials and methods, our set of mAbs mainly detects bound versus unbound integrins, roughly corresponding with extended/open versus bent/closed conformations, i.e., "active" versus "inactive" integrin β1 subpopulations. Moreover, mAb AIIB2 competed for binding with the fibronectin FN3 domain-10 (Fig. S1 A), indicating that AIIB2 recognizes a ligand-attenuated binding site (LABS), selectively labeling nonligand-bound β1 integrins.

We compared the distributions of active versus inactive β1 integrin subpopulations by STED imaging. We found that both active (9EG7 or 12G10) and inactive (AIIB2 or mAb13) integrin β1 antibodies (abs) decorated nanoclusters within FAs (Fig. 2, A and B; and Fig. S1 B). Interestingly, paxillin was recently shown to localize in nanoscale linear arrays within FAs (Hu et al., 2015). We assessed whether β1 integrin nanoclusters, which (unlike paxillin) directly mediate cell–ECM attachment, also localize in linear patterns, and whether such arrangements depend on integrin conformation. To this end, we blindly scored individual FAs for the presence of linearly aligned nanoclusters after labeling with the mAbs K20 (total integrin β1), 9EG7, or 12G10 (active integrin) or AIIB2 or mAb13 (inactive integrins; Figs. 2 C and S1 C). Both total and active β1 integrin displayed linear substructures in >65% of FAs. This suggests that FAs are organized hierarchically, with active β1 integrin nanoclusters aligning to form linear structures that in turn build FAs. In contrast, only ∼30% of inactive β1-labeled FAs displayed linear nanocluster arrangements (Figs. 2 C and S1 C). Moreover, automated quantitative image analysis based on random sample consensus (RANSAC), an iterative algorithm for inlier/outlier determination (Fischler and Bolles, 1981), verified that active β1 integrins appeared in linear patterns to a higher degree than inactive β1 within FAs. This is shown by the larger number of lines needed to fit a similarly large cohort of nanoclusters labeled with mAb AIIB2 compared with mAb 9EG7, which also displayed a larger number of nanoclusters fitted per line (Fig. 2 D). The fact that robust even if not large differences appear when applying this analysis to our images reveals a substantial difference in intra-FA cluster arrangement given the unsupervised nature of the algorithm. Considering that fibronectin, used as substratum in this study, forms fibrils (Singh et al., 2010), ECM–fibril binding suggests a possible explanation for why active (ECM-bound) integrins frequently form linear nanocluster arrays. Likewise, FAs contain parallel F-actin fibrils (Burridge and Guilluy, 2016), and thus considering F-actin linkage to ECM-bound integrins, linear patterns of bound integrins may also arise along F-actin fibrils.

By STED, active β1-integrin nanoclusters displayed lower nearest neighbor distance (NND; Fig. 2 E) and, importantly, significantly lower NND variance, implying a more regular nanocluster spacing as compared with inactive β1 integrin counterparts (Fig. 2 E). Also, STORM detected both active and inactive integrin nanoclusters (Fig. 2, F and G). In congruence with STED analyses, STORM data indicated that active β1 integrin nanoclusters localized closer together, which may reflect their higher density (Fig. S1 D). Remarkably, and also consistent with STED analysis, active β1 integrin nanoclusters displayed significantly less variance in NND than inactive integrin nanoclusters (Fig. 2 H). Thus, data derived from two distinct superresolution imaging modalities confirm that active integrin nanoclusters are tightly and regularly organized, including arrangement into linear FA substructures. In contrast, inactive integrin nanoclusters are less organized, with more variability in their spacing and lower frequency of linear arrangements. Considering the existence of intra-FA integrin subpopulations with distinct dynamics (stationary versus rapid diffusion; Rossier et al., 2012; Rossier and Giannone, 2016), we hypothesize that tightly ordered active β1 integrin nanoclusters may correspond with stationary ECM-bound integrin subpopulations, whereas inactive β1 integrin nanoclusters, probably largely ECM unbound, may be more mobile, resulting in a more variable organization.

Although all comparisons of active and inactive integrins revealed trends that were consistent between STED and STORM data, absolute nanocluster size and NND values measured by STORM were smaller than those measured by STED. These differences mirror the higher resolution of STORM versus STED, with STORM enabling measurements on shorter length scales. Similarly, differences in analytical methodologies, with different

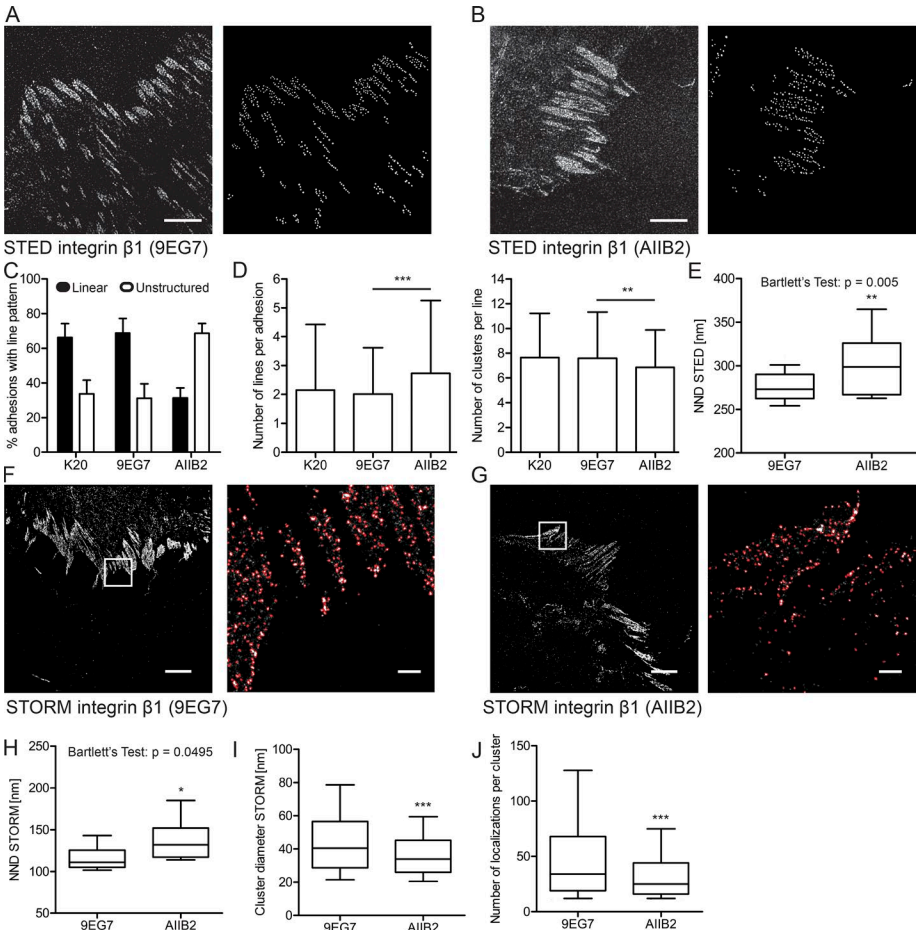

Figure 2. **Distinct organization of active and inactive β1 integrin nanoclusters within FAs. (A)** Left: Representative STED image of an Hs578T cell labeled with antiactive β1 integrin mAb 9EG7 (rhodamine). Right: Spatial distribution of detected intensity peaks within FAs. **(B)** Left: Representative STED image of Hs578T cells labeled with antiinactive β1 integrin mAb AIIB2 (rhodamine). Right: Spatial distribution of detected intensity peaks within FAs. **(C)** Bars show FAs scored for linear versus unstructured patterns in labelings of mAbs K20 (n = 23 images), 9EG7 (n = 21 images), and AIIB2 (n = 18 images), displayed as mean percentages ± SEM. **(D)** Automated linearity analysis. Left: Means ± SD of fitted RANSAC lines needed to deplete all segmented clusters per FA for K20 (n = 13 cells), 9EG7 (n = 11 cells), and AIIB2 (n = 11 cells) labelings. Right: Mean ± SD number of clusters per fitted RANSAC line for the same experimental set. Kolmogorov-Smirnov test: *, P < 0.05; **, P < 0.01. **(E)** Bars show median NND (quartile distribution in boxes; decile distributions in whiskers) of STED-identified clusters for mAb 9EG7 (n = 19 images) and mAb AIIB2 (n = 19) labelings within FAs. The two distributions display different variances. **(F and G)** Left: Representative STORM image of Hs578T cells labeled with mAb 9EG7 (F) or mAb AIIB2 (G; Alexa Fluor 405 through Alexa Fluor 647). White boxes indicate zooms shown on right. Red circles show DBSCAN-identified clusters in zoomed areas. Bars: (A, B, F, and G,main images) 5 µm; (F and G, insets) 500 nm. **(H)** Error bars show median NNDs (quartile distribution in boxes; decile distribution in whiskers) of β1 integrin clusters in STORM images of mAb 9EG7 (n = 12 images) and mAb AIIB2 (n = 14 images) labeling. The two distributions display different variances. **(I and J)** The bars show median cluster size (I) and median number of cluster localizations (J) of STORM images (quartile distribution in boxes; decile distribution in whiskers) of mAb 9EG7 (n = 14 images) and mAb AIIB2 (n = 14) labeling within FAs. t test: *, P ≤ 0.05; **, P ≤ 0.01; ***, P ≤ 0.001.

signal-to-noise ratio sensitivities (DBSCAN-based localization clustering for STORM; intensity-based segmentation for STED) can contribute to the observed differences in nanocluster size and organization (Deschout et al., 2014; Shivanandan et al., 2014). Nonetheless, collectively, STORM and STED data clearly indicate that active and inactive β1 integrin subpopulations are distinctly organized within FAs.

STED-analyzed nanocluster diameter was larger for active than for inactive nanoclusters, corresponding in STORM with a difference in number of localizations per cluster (Fig. 2, I and J; and Fig. S1 E). Moreover, STED also detected small, sparse clusterlike labeling outside of FAs, less densely labeled than nanoclusters in FAs (Fig. S1 E). This labeling outside FAs may detect integrin clusters in smaller organizational arrangements and may also include unspecific labeling.

Unsurprisingly, both STORM and STED revealed significant variability in nanocluster size and labeling density. Importantly, to estimate the labeling density per cluster, we used a standard STED sample boasting the same number of dye molecules as a secondary ab (Schmied et al., 2012). STED imaging indicated that mAb K20 (total β1 integrins)–labeled nanoclusters contained on average ∼10 times the labeling of a single secondary ab (Fig. S1 F), whereas the mean number of mAb K20 localizations per STORM-detected nanocluster was approximately sixfold of that detected with a single mAb K20 attached to glass (Fig. S1 G). Based on these results, we are confident that the nanoclusters are not solely caused by the blinking of fluorophores or unspecific single secondary ab labeling but instead arise from multiple detected integrin molecules clustered together.

Considering that the maximum distance between integrin molecules at which integrin clustering can occur is ∼45 nm (Roca-Cusachs et al., 2009; Le Saux et al., 2011) as well as the mean cluster size detected for STED and STORM, we can conclude that we detect more β1 integrin molecules per nanocluster than the minimum number required to facilitate integrin clustering. We titrated the labeling conditions to saturate the signal, and in STORM, we used exhaustive fluorophore blinking. If we would assume that our integrin labeling was close to saturation, a rough estimate would suggest that there is a mean of six or more β1 integrins per nanocluster. However, the precise number of molecules cannot be determined by our use of STED and STORM because of inherent uncertainties (Blom and Widengren, 2017) including our inability to control for precise labeling saturation and primary-to-secondary ab stoichiometry.

Segregation of active and inactive β1 integrin subpopulations

We next imaged FAs at different resolutions and calculated the Pearson's correlation coefficient to estimate the degree of colocalization of active and inactive β1 integrin subpopulations within FAs (Fig. 3, A–E; and Fig. S2 A). The suitability of the Pearson's correlation coefficient for colocalization of ab-labeled targets by superresolution microscopy has been previously demonstrated (Xu et al., 2016). In conventional microscopy, the extent of colocalization is typically overestimated because of the limited resolution. Conversely, at superresolution, underestimation of colocalization may occur if the resolution is close to the size of the labels (Xu et al., 2016). We estimated the upper limit of colocalization achieved with each microscopy technique by labeling cells with a single primary ab (12G10, AIIB2, or K20) followed by simultaneous labeling with two distinctly labeled secondary abs (one-primary and two-secondary control; Fig. 3, B–E). We obtained Pearson's correlation coefficients for maximal overlap consistent with previous studies of each of the techniques (Neumann et al., 2010; Xu et al., 2016).

To assess the robustness of the observed colocalization between active and inactive β1 integrins, we used combinations of mAbs targeting different integrin subpopulations (mAbs 9EG7, 12G10, and Huts-4 for active β1 integrins; mAbs AIIB2 and mAb13 for inactive β1 integrins; Table 1). Colabeling mAb 9EG7 with mAb 12G10 or mAb Huts-4 resulted in a high degree of colocalization, indistinguishable from the maximum expected for STED (one-primary two-secondary control), indicating that these three mAbs label the same active β1 integrin subpopulation (Fig. 3 E). The degree of colocalization between mAb K20 (total β1 integrin) and either mAb 9EG7 (active) or mAb AIIB2 (inactive) was relatively high (Fig. 3 E), although it was significantly lower than that obtained with two different mAbs for active β1. This is consistent with the mAbs 9EG7 and AIIB2 labeling subsets of the total K20-labeled β1 integrin population.

Having confirmed the expected labeling patterns among this suite of abs, we measured colocalization between active and inactive β1 integrins using images obtained by confocal, STED, and STORM microscopy (Fig. 3, A–E; and Fig. S2 A). Confocal images of mAb AIIB2 (inactive) and 12G10 (active) colabelings elicited Pearson's correlation coefficient close to the maximal possible overlap achieved via 12G10 double labeling (Fig. 3 B). However, the same labeling combination assessed with the higher STED resolution produced a Pearson's coefficient close to zero (Fig. 3 C), indicating that the high colocalization observed in the confocal images is a false positive because of their limited resolution. This also shows that these mAbs indeed label different integrin β1 subpopulations and that surprisingly, active and inactive β1 integrins are nearly exclusive in their relative spatial distribution. Pearson's coefficients between active and inactive β1 integrins obtained by STORM imaging were even lower (Fig. 3 D) as expected when assessing colocalization at higher resolution (10 nm rendering; Xu et al., 2016). Alternative rendering of STORM localizations with a precision (50 nm) matching STED image resolution yielded Pearson's coefficients similar to those recorded for STED images (Fig. 3 D).

We then combined several additional active versus inactive anti–β1 integrin mAb pairs imaged by STED microscopy. These pairs included mAb AIIB2 (inactive β1) with mAb Huts-4 (active β1) as well as mAb 13 (inactive β1) with mAb 12G10 or mAb Huts-4 (active β1). Consistent with the originally observed segregation (Fig. 3 C), each of these three additional active versus inactive integrin colabeling pairs displayed very low colocalization (Fig. 3 E). To exclude that this lack of colocalization may reflect mAb competition, as indicated for some of these mAb combinations in unfixed cells by FACS (Su et al., 2016), we performed FACS mAb competition analysis on fixed cells labeled with protocols equivalent to our microscopy analyses. Crucially, we did not detect any significant mAb competition (Fig. S2 B). This is consistent with the notion that the indicated integrin β1 mAb competition is predominantly caused by mAb-induced allosteric integrin conformation alterations (Su et al., 2016), and thus abolished under our experimental conditions by cell fixation.

Ab-based labeling has been successfully applied in numerous superresolution studies (French et al., 2016; Sidenstein et al., 2016). We considered this as the best available option for determining the distribution of active versus inactive integrins because the precise nanoorganization of FAs may be perturbed by overexpression of fluorescently tagged proteins (Snapp, 2005). Such overexpression may also alter naturally occurring equilibria in integrin conformations that are central to this study. Although ab labeling carries limitations (Fornasiero and Opazo, 2015), we neutralize many of these by relating all colocalization comparisons to an inherent control: single primary ab with two differently labeled secondary ab labelings. This is significant because we focus on relative differences and trends in colocalization values, reducing the influence of absolute levels of epitope binding, secondary ab localization uncertainty, or the particular method of colocalization measurement. Also, most nanoclusters identified by STORM and STED were larger than what could be explained by potential secondary ab clustering. Furthermore, variability in ab specificity was mitigated through the use of multiple active- and inactive-specific mAbs in several pair combinations for colocalization analyses (four active versus inactive β1 integrin–labeling combinations comprising three active- and two inactive-specific mAbs). In all cases, we recorded highly consistent evidence for the spatial segregation of active and inactive β1 integrins within FAs.

Importantly, and consistent with the pixel-based colocalization data, the number of nanoclusters that displayed any overlap between active (12G10) and inactive (AIIB2) β1 integrin was significantly lower than the maximum obtained for mAb K20 double labeling, whereas colabeling of mAb K20 (total β1 integrin) with either active or inactive integrins produced expected intermediate nanocluster overlap values (Figs. 3 F and S2 C). We thus provide direct evidence that active and inactive β1 integrins are at least partially segregated into distinct nanoclusters.

Nanocluster-scale segregation of active and inactive β1 integrins has important new implications for the regulation of integrin activity. So far, integrin activity regulation has been largely considered to operate at the scale of individual integrins. However, if individual integrin activity states were independently regulated, active and inactive integrins would be interspersed within nanoclusters and therefore highly colocalized. Instead, by demonstrating segregation of active and inactive integrins into distinct nanoclusters, we present evidence suggesting a novel mechanism that locally coordinates and synchronizes integrin

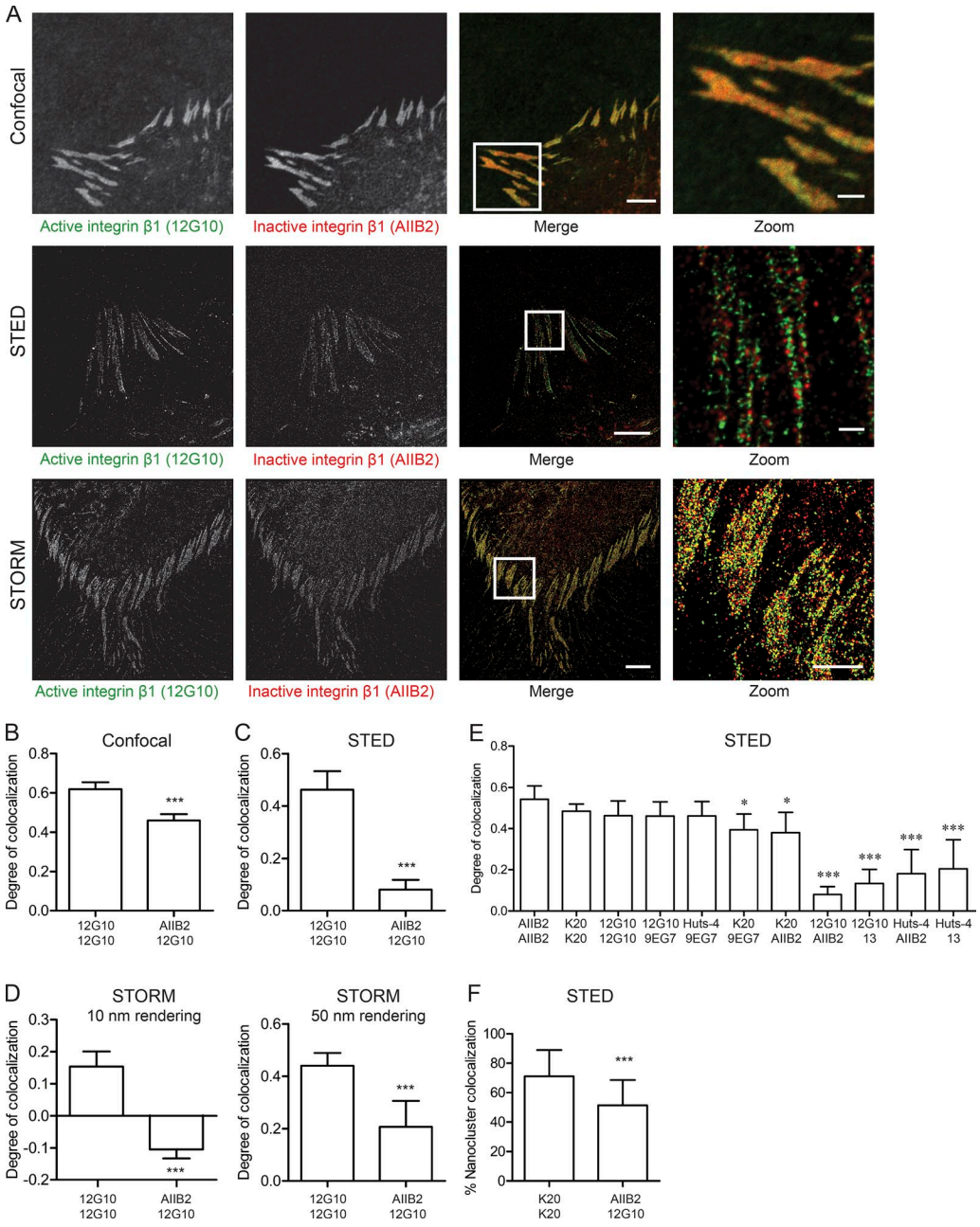

Figure 3. **Distinct localization of active and inactive β1 integrins within FAs. (A)** Representative confocal, STED, and STORM images of Hs578T cells colabeled with antiactive β1 integrin mAb 12G10 (OG488 or Cy3; Alexa Fluor 647) and antiinactive β1 integrin mAb AIIB2 (rhodamine or Alexa Fluor 405 through Alexa Fluor 647). White boxes indicate zoomed areas on the right. Bars: (main images) 5 µm; (insets) 2 µm. **(B–D)** Bars show mean Pearson's correlation coefficients (± SD) obtained by confocal (B), STED (C), and STORM (D) images colabeled with mAb 12G10 and mAb AIIB2. Confocal, *n* = 10 images; STED, *n* = 20; STORM, *n* = 6. mAb 12G10 labelings targeted by two differently colored secondary abs were used as control for maximal colocalization. Confocal, *n* = 9 images; STED, *n* = 13; STORM, *n* = 6. **(E)** The three left bars show Hs578T cells labeled by mAbs AIIB2 (*n* = 18 images), K20 (*n* = 11), or 12G10 (*n* = 13) targeted with two differently colored secondary abs each as controls for maximal colocalization. The remaining bars show mean Pearson's correlation coefficients (± SD) of STED images of Hs578T cells colabeled by mAb 12G10 and mAb 9EG7 (*n* = 12 images); mAb Huts-4 and mAb 9EG7 (*n* = 11); mAb K20 and mAb 9EG7 (*n* = 14); mAb K20 and mAb AIIB2 (*n* = 17); mAb 12G10 and mAb AIIB2 (*n* = 20); mAb 12G10 and mAb 13 (*n* = 11); mAb Huts-4 and mAb AIIB2 (*n* = 11); and mAb Huts-4 and mAb 13 (*n* = 5). The individual colocalizations were statistically compared with the control with the lowest coefficient (12G10), providing the most stringent comparison. The mAb AIIB2 versus mAb12G10 combination was duplicated from C to facilitate direct comparison. **(F)** Bars show mean percentages ± SD of overlapping nanoclusters segmented in STED images of Hs578T cells colabeled with mAb 12G10 and mAb AIIB2 (*n* = 20 images). Hs578T cells labeled using mAb K20 and two differently colored secondary abs both targeting mAb K20 were used as control for maximal overlap. *n* = 9 images. *t* test: *, P ≤ 0.05; ***, P ≤ 0.001.

activity states. The existence of a coordinating mechanism for integrin activity regulation within nanoclusters represents a fundamentally new concept and may contribute to a better understanding of how FAs form and function.

Many plasma membrane proteins cluster at the nanoscale level (Goyette and Gaus, 2017). Although passive reorganization has been shown to lead to colocalization of proteins with similar ectodomain sizes, Paszek et al. (2014) introduced the

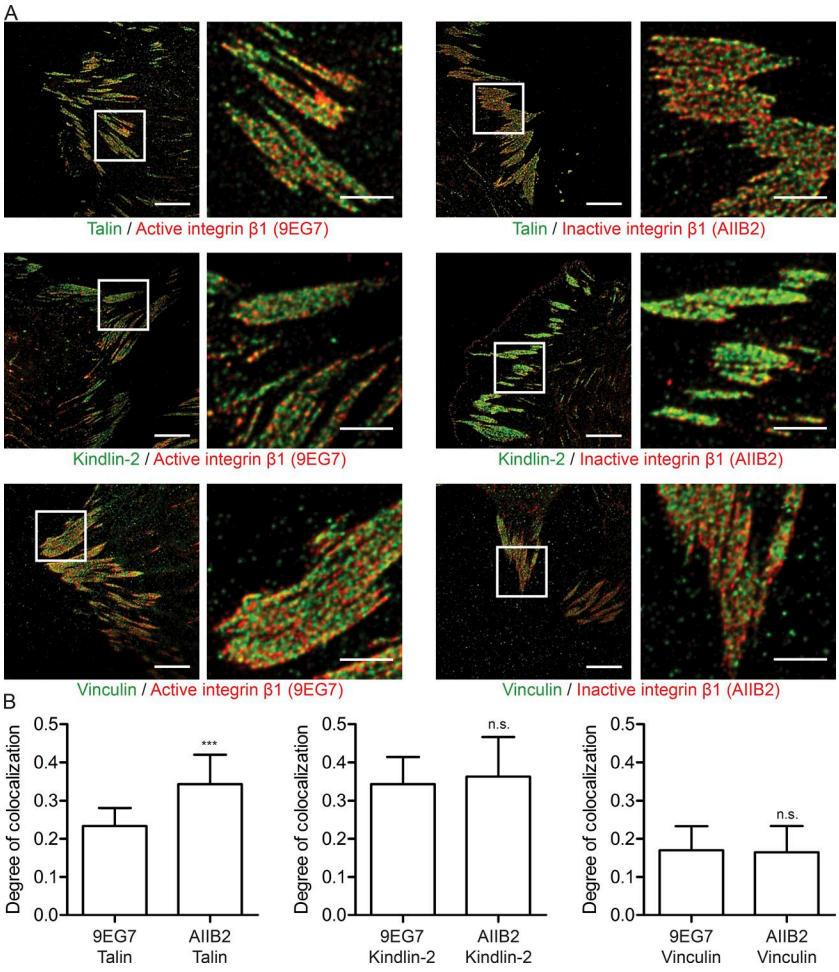

Figure 4. **Colocalization of talin, kindlin-2, and vinculin with active and inactive β1 integrins within FAs. (A)** Left: Representative STED images of Hs578T cells labeled with antiactive β1 integrin mAb 9EG7 (left) or antiinactive β1 integrin mAb AIIB2 (right; both rhodamine) and antitalin mAb, anti–kindlin-2 polyclonal ab, or antivinculin polyclonal ab (all OG488). White boxes indicate zoomed areas. Bars: (main images) 5 µm; (insets) 2 µm. **(B)** Bars show mean Pearson's correlation coefficients (± SD) of STED images of Hs578T cells colabeled as indicated. $n = 10–11$ images for each combination. *t* test: ***, $P \le 0.001$.

kinetic trapping model for passive segregation of bound and unbound integrins mediated by biophysical properties of the glycocalyx (Köhler et al., 2010). In this model, the binding of a first integrin brings the ECM closer to the cell, thereby enabling adjacent integrins to also bind (Paszek et al., 2014). Considering that ECM-bound integrins are activated, this model provides a plausible mechanism for the spatially coordinated control of integrin activity reported in this study. However, the evidence presented by Paszek et al. (2014) focuses on length scales considerably larger than those associated with nanoclusters. Hence the detailed mechanism or mechanisms accounting for collective integrin activity state segregation remains unclear.

Talin, kindlin-2, and vinculin colocalize with both active and inactive β1 integrins

We next analyzed the nanocluster distributions of core adhesome components with roles in integrin activity regulation. We examined the colocalization of active (9EG7) or inactive (AIIB2) β1 integrin subpopulations with talin, kindlin-2, or vinculin using STED microscopy, estimating Pearson's correlation coefficient in segmented FAs. Interestingly, talin, kindlin-2, and vinculin all colocalized moderately with both active and inactive β1 integrins (Fig. 4, A and B; and Fig. S3), indicating their association with active and inactive nanoclusters. This may correspond with previous evidence that preassembled multiprotein adhesome building blocks are recruited to FAs (Hoffmann et al., 2014), where they might precipitate ligand-independent assembly of integrin nanoclusters.

In conclusion, our results provide significant new insights into the nanoscale molecular architecture of FAs by revealing the spatial segregation of active and inactive β1 integrin nanoclusters as well as corresponding differences in the spatial organization of these integrin subpopulations. Functionally, the nanocluster-scale segregation of active and inactive integrins implies the existence of a new coordinate regulatory mechanism that promotes local synchronization of integrin activity states within integrin nanoclusters. Understanding the precise mechanism of this coordinate regulation now appears as a crucial question in the context of understanding cell–ECM adhesion formation, function, and regulation.

Materials and methods

Abs

Primary abs used for immunostaining were rat anti–β1 integrin mAb 9EG7 (BD; Lenter et al., 1993; Bazzoni et al., 1995; Su et al., 2016), mAb 13 (BD; Akiyama et al., 1989; Mould et al., 1996; Su et al., 2016), and mAb AIIB2 (Developmental Studies Hybridoma Bank; Werb et al., 1989; Takada and Puzon, 1993; Park et al., 2008); mouse anti–β1 integrin mAb K20 (Santa Cruz Biotechnology, Inc.;

Amiot et al., 1986; Takada and Puzon, 1993), mAb Huts-4 (Chemicon; Luque et al., 1996; Su et al., 2016), and mAb 12G20 (Abcam; Mould et al., 1995; Su et al., 2016); mouse antitalin mAb 8d4 (Sigma-Aldrich); and rabbit polyclonal abs antivinculin (V4139; Sigma-Aldrich) and anti–kindlin-2 (ab74030; Abcam). All secondary abs used were depleted for cross-reactivity. Secondary abs goat anti–mouse coupled to Oregon green 488 (O-11033; Thermo Fisher Scientific) or rhodamine red-X (115-295-146; Jackson ImmunoResearch Laboratories, Inc.), goat anti–rat coupled to rhodamine red-X (112-295-167; Jackson ImmunoResearch Laboratories, Inc.), and goat anti–rat coupled to Oregon green 488 (O-6382; Thermo Fisher Scientific) were used. Secondary abs for STORM imaging were donkey anti–rat (712-005-153; Jackson ImmunoResearch Laboratories, Inc.) and goat anti–mouse IgG (A16080; Thermo Fisher Scientific) labeled in house with different combinations of activator/reporter pairs as previously described (Bates et al., 2007). In brief, the dyes were purchased as *N*-hydroxysuccinimide ester derivatives: Alexa Fluor 405 carboxylic acid succinimidyl ester (Invitrogen), Cy3 monoreactive dye pack (GE Healthcare), and Alexa Fluor 647 carboxylic acid succinimidyl ester (Invitrogen). Ab labeling reactions were performed by incubating for 40 min at RT a mixture containing the secondary ab $NaHCO_3$ and the appropriate pair of activator/reporter dyes diluted in DMSO. Purification of labeled abs was performed using NAP5 columns (GE Healthcare). The dye/ab ratio was quantified using NanoDrop (Thermo Fisher Scientific), and only abs with a composition of three to four Alexa Fluor 405 or Cy3 and 0.9–1.5 Alexa Fluor 647 per ab were used for imaging.

Specificity of mAbs for active and inactive β1 integrin conformations

mAbs 9EG7, 12G10, and Huts-4 recognize epitopes hidden in the bent integrin β1 conformation. Instead, these mAbs bind only to β1 integrin in extended conformations as induced by ligand binding or manganese stimulation (Bazzoni et al., 1995). We therefore refer to the β1 integrin subpopulation labeled by mAbs 9EG7, 12G10, and Huts-4 as active β1 integrins, with the mAbs 12G10 and Huts-4 also being specific for the extended/open high-affinity integrin conformation (Luque et al., 1996; Mould et al., 1996; Su et al., 2016). We also used the anti–β1 integrin mAb AIIB2, which binds to an epitope in the βA domain, which functionally blocks cellular attachment to fibronectin (Werb et al., 1989) and also competes for binding with the fibronectin FN3 domain-10 (Fig. S1 A). This competitive binding indicates that AIIB2 recognizes a LABS and therefore that AIIB2 binds selectively to nonligand-bound β1 integrins. Indeed, AIIB2 has previously been shown to label inactive β1 integrins (Werb et al., 1989; Takada and Puzon, 1993; Park et al., 2008). Similarly, mAb13 has been shown to recognize a closed, nonligand-bound β1 integrin conformation with limited ligand affinity (Mould et al., 1996; Su et al., 2016). For simplicity, we use in this study the term "inactive" to describe all β1 integrins labeled by either mAb AIIB2 (unbound integrin) or mAb13 (closed unbound integrin). It may be argued that 9EG7, AIIB2, and mAb13 may recognize unbound integrins in the extended/closed conformation. However, given that the extended/closed conformation represents only ∼0.15% of unbound α5β1 integrins (Li et al., 2017), we expect virtually no overlap between the integrin subpopulations detected with these abs. Also, given that the extended/open conformation is energetically favorable compared with the extended/closed conformation and has >5,000× higher affinity for fibronectin (Li et al., 2017), the enrichment of extended integrins in attached cells can be mainly attributed to ECM-binding stabilization of the extended/open integrin conformation. Thus, in attached cells, mAb 9EG7 should predominantly label bound extended/open integrins. Therefore, with our set of mAbs, we mainly detect bound versus unbound integrins, roughly corresponding with extended/open versus bent/closed conformations, i.e., active versus inactive integrin β1 subpopulations.

Immunolabeling for imaging

Hs578T cells forming prominent FAs were grown in DMEM supplemented with 10% FBS at 5% CO_2 and 37°C. Before imaging, cells were replated onto fibronectin-coated (20 µg/ml fibronectin) glass-bottomed imaging dishes (MatTek Corporation) for 4 h at a density of 5,000 cells/cm^2 to avoid ECM remodeling. Cells were washed twice in PBS before fixation and permeabilization for 10 min in 2% paraformaldehyde and 0.1% Triton X-100, an optimized fixation procedure to preserve adhesion structures, followed by three washes with PBS and blocking at 4°C in 0.5% BSA (or goat serum for antitalin staining) overnight. Primary abs were diluted in PBS with 0.5% BSA and then incubated simultaneously for 30 min at 4°C and for 1 h at RT. Samples were washed five times with PBS, incubated for 1 h with secondary ab diluted in PBS plus 0.5% BSA, and washed five times with PBS. To obtain optimal staining, saturating ab concentrations were determined empirically by titration. For STORM experiments, the following ab concentrations were used: 9EG7 (1 µg/ml), 12G10 (40 µg/ml), and AIIB2 (1 µg/ml). For STED and confocal microscopy, the following ab concentrations were used: K20 (50 µg/ml), 12G10 (40 µg/ml), 9EG7 (8 µg/ml), Huts-4 (250 µg/ml), AIIB2 (6 µg/ml), mAb13 (25 µg/ml), antivinculin (33 µg/ml), antitalin (178 µg/ml), and anti–kindlin-2 (26 µg/ml).

Microscopy

Prominent FAs are readily recognizable and were identified by eye and selected for image acquisition. Confocal images were acquired with an A1R confocal microscope (Nikon) using an oil-immersion Plan Apochromat 60× objective (1.40 NA) at RT. STORM images were acquired at 21°C with an N-STORM commercial system mounted on a T*i*E inverted microscope (Nikon), fitted with a STORM-capable TIRF illuminator, and coupled to an iXon 897 electron-multiplying charge-coupled device camera (512 × 512 active pixels; Andor Technology) using a collar-optimized CFI Apochromat TIRF 100× 1.49 NA objective. The LU4A laser launch was also acquired from Nikon and nominally delivers 300 mW at 647 nm, 50 mW at 561 nm, 40 mW at 488 nm, and 100 mW at 405 nm. NIS Elements AR 4.30.02 software (Nikon) was used. For single-color imaging, 647-nm laser light was used for exciting the reporter dye (Alexa Fluor 647) and switching it to the dark state, and 405- or 561-nm laser light was used for reactivating Alexa Fluor 647 into a fluorescent state via an activator dye (Alexa Fluor 405 or Cy3). An imaging cycle comprised one frame of activation alternated with four frames of reporter imaging. Dual-color imaging was performed by alternating 405-activated

cycles and 561-activated cycles. Imaging was done using a previously described buffer containing 100 mM mercaptoethylamine, 0.5 mg/ml glucose oxidase, 40 µg/ml catalase, and 5% glucose (Sigma-Aldrich) in PBS (Bates et al., 2007).

STED images were acquired at RT with LASX software using an SP8 3× STED system (Leica Microsystems) equipped with lasers for depletion of fluorophores emitting in the blue/green (592 nm; MPB Communications Inc.), orange (660 nm; Laser Quantum), and red/far red (775 nm; OneFive GmbH). A pair of depletion-wavelength (660/592) or a single-wavelength (660) laser was applied for multicolor STED imaging. A chromatically optimized oil-immersion objective (high-contrast Plan Apochromat 100× 1.40 NA oil STED white; Leica Microsystems) was used for imaging, and a tunable pulsed white light fiber laser emitting in the 470–670-nm spectrum was applied for excitation. Selected wavelengths were 488 nm for Oregon green 488 and 575 nm for rhodamine red-X. Fluorescence signals were passed through a 0.8–0.9-Airy-unit pinhole, a dichroic mirror optimized for each STED laser, including notch filters placed in front of sensitive photodetectors (Leica Hybrid Detectors). Dual-color frames (1,024 × 1,024 pixels) were acquired sequentially frame by frame at a scan speed of 400 lines per second with four line averages and a pixel size of 25 nm. Precision calibrations were done on 40-nm fluorescent beads (FluoSpheres; Invitrogen) spin coated onto the glass surface of a coverslip and mounted in Mowiol. Resolved lateral full width at half maximum values of 42 ± 3 nm (n = 30) were achieved (excitation, 635 nm, and depletion, 750–775 nm), pointing to STED focal widths of ≤40 nm.

Image analysis

Raw STED images were deconvolved using Huygens Professional software (Scientific Volume Imaging; Schoonderwoert et al., 2013) with a STED-specific algorithm using a computationally distilled point-spread function. Values for objective NA and oil refractive index were input. Intensity peaks in STED images were obtained by the Imaris (Bitplane) module ImarisCell. With this module, adhesions were segmented based on automated intensity thresholding and a minimal size of 1 µm, and thresholded objects were identified within the adhesion. Line-intensity profiles were generated with ImageJ (National Institutes of Health) using a line width of 10 pixels. Scoring of individual adhesions for linear or unstructured patterns was performed manually. STORM images were analyzed using custom-written software (Insight3; provided by B. Huang, University of California, San Francisco, San Francisco, CA) by fitting the point-spread function of individual fluorophores with a simple Gaussian curve in every frame to determine their x and y coordinates. The intensity threshold for considering a blink was set at 700–1,000 grayscale levels (on 16-bit images), whereas the minimum acceptable sphericity was set at 0.8. STORM images were rendered with a 10-nm localization precision based on the mean number of photons emitted per switching event of the Alexa Fluor 647 fluorophore were used, if not stated otherwise (Dempsey et al., 2011). Clusters in STORM images were identified by the DBSCAN algorithm (minimal number of points = 10; radius [ε] = 20 nm) integrated in Insight3. NNDs were calculated with MATLAB (MathWorks).

Integrin cluster size was determined in STED deconvolved images after segmentation. Regions of interest were drawn around FAs based on confocal images. Using these regions of interest as a mask, STED images were subjected to segmentation by applying the ImageJ plugin Robust Automatic Threshold Selection, setting 50 grayscale levels as noise threshold for all analyzed images. The radius of each segmented cluster was obtained upon cluster analysis using ImageJ Object Analysis functionality, and objects with radius <25 nm (therefore below our resolution limit) were excluded from the analysis.

Automatic linearity analysis was performed by applying the iterative RANSAC algorithm on Imaris-segmented, deconvolved STED images. The RANSAC algorithm, a nondeterministic approach for inlier/outlier determination (Fischler and Bolles, 1981), was implemented in Python. FAs were segmented using Imaris, and the clusters within the perimeter of each FA were processed using the RANSAC algorithm. At each iteration, the RANSAC algorithm drew a line between two randomly selected clusters within the distribution. The number of inlier clusters close to this line and the number of outlier clusters distant to the line were measured. The process was repeated 1,000 times until the optimum line (that with the most inliers) was found. Once fit, the inlier clusters were removed from the distribution, and the remaining clusters were analyzed in the same way. Inliers were determined as those within ≥3 pixel distance of the line. A minimum of four inlier clusters was required for a fit to be accepted, and the process was repeated 20 times to ensure the possibility that multiple lines per FA were drawn. In other words, the algorithm fits a line matching as many nanoclusters as possible in the first round, and in following rounds, it would fit the remaining clusters with decreasing correlation coefficients until all clusters were fitted. If FAs had nanoclusters organized in linear patterns, a few lines would suffice to fit all detected clusters. If these clusters were dispersed, more iterations would have been needed until all clusters were fitted. Kolmogorov-Smirnov tests were applied to determine statistically significant differences between distributions.

Colocalization analysis of confocal and STED images was performed using the Imaris module ImarisColoc. With this module, adhesions were segmented based on automated intensity thresholding, and thresholded Pearson's correlation coefficients were calculated. Pearson's coefficient values ranged from 1 for a perfect, linear, and positive correlation to –1 for a perfect, linear, and negative/inverse correlation (Dunn et al., 2011). Colocalization analysis of STORM images was performed using the ImageJ plugin Coloc2. Prominent FAs were manually segmented, and thresholded Pearson's correlation coefficients were calculated. Percent overlap was calculated as the percentage of intensity peaks within STED images that had a neighboring intensity peak of a different labeling within a distance of 200 nm, which corresponds with the median radius of the intensity peaks as measured by Imaris.

Determination of cluster intensity by calibration with Gattaquant standard sample

Single goat anti–mouse secondary abs incorporate six to seven Oregon green 488 dye molecules according to the manufacturer's

indications (O-11033; Thermo Fisher Scientific). To mimic single ab labeling, standard Gattaquant DNA STED nanorulers with two dye-binding localizations separated by 90 ± 5 nm were custom labeled with six to seven Oregon green 488 dye molecules per binding site and mounted on high-quality N1.5 optical glass by the manufacturer. This customized Gattaquant sample was imaged with the same STED settings used for imaging ab-based cell labelings. Intensities obtained from imaging the Gattaquant standard in STED mode were used to determine mean cluster labeling in STED images based on the linear relationship between intensity and dye density.

Regions of interest with a diameter of 50 nm (equivalent to the smaller cluster size detectable with STED) matching the size of Gattaquant sample labeling locations were drawn on representative STED images of the Gattaquant ruler sample, and the mean intensity of the region of interest was examined using the Measure function in ImageJ. Similarly, 50-nm-diameter regions of interest were drawn in representative STED images of K20 cell stainings, and intensities were compared.

Determination of numbers of integrin localizations per STORM cluster

mAb K20 was adsorbed on glass-bottomed imaging dishes (MatTek) for 30 min at RT and then diluted 10^5 times in PBS + 0.5% BSA to promote individual ab adsorption. Secondary ab (Alexa Flour 405/647 labeled) staining and STORM imaging settings used were identical as for ab-based cell labeling. Clusters in STORM images of mAb K20 on glass and mAb K20–labeled FAs in cells were identified by the DBSCAN algorithm (minimal number of points = 2; radius [ε] = 20 nm) integrated in Insight3. The mean numbers of localizations were compared with estimates of the number of integrin labels per nanocluster within FAs.

Flow cytometry

For fibronectin, Hs578T cells were trypsinized and washed once in PBS + 5% BSA. Cells were incubated in PBS + 5% BSA with or without the 20 µg/ml recombinant human fibronectin FN3 domain-10 (LD Biopharma, Inc.) on ice for 2 h at 10^6 cells/ml before fixation with 2% paraformaldehyde for 10 min at RT. Cells were incubated with mAbs AIIB2 (0.5 ng/ml) or K20 (1 µg/ml) for 45 min, washed once with PBS + 5% BSA, and stained with anti–rat OG488 or anti–mouse phycoerythrin ab (1:200) for 30 min before analysis by FACS (FACSCalibur; BD). Median fluorescence intensities were used to calculate the percentage of bound ab with fibronectin competition.

To test potential mAb competition, Hs578T cells were trypsinized and washed once in PBS + 1% BSA before fixation with 2% paraformaldehyde for 10 min at RT. Cells were incubated with one or two primary abs for 45 min, washed twice with PBS + 1% BSA, and incubated with the secondary abs anti–rat OG488 (1:200) and anti–mouse phycoerythrin (1:200) for 30 min at RT before analysis by FACS (FACSCalibur). Median fluorescence intensities were used to calculate the ratio between mAb labeling in the presence of a second mAb divided by the labeling intensity obtained by single mAb labeling alone. Compensation for bleedthrough and cross-reactivity between secondary abs were considered and withdrawn. The following primary ab concentrations were used: AIIB2 (6 ng/ml), 12G10 (40 ng/ml), Huts-4 (250 ng/ml), and mAb13 (40 ng/ml).

Online supplemental material

Fig. S1 shows β1 integrin cluster characterization, indicating first the degree of linearity of 12G10- and mAb13-labeled integrin clusters as an alternative to 9EG7 and AIIB2 labels shown in Fig. 2 C. In addition, along with cluster density estimation for STORM, cluster size spread for K20, 9EG7, and AIIB2 abs for STED imaging was analyzed. These datasets complement Fig. 2 (E and H), providing a detailed picture on nanocluster distribution. Moreover, quantification of the minimum number of integrin molecules per K20-labeled cluster along with the corresponding controls is presented for both STORM and STED. Fig. S2 strengthens colocalization data for the different integrin-labeling abs, showing a panel with different ab combinations for active (9EG7, 12G10, and HUTS4), inactive (AIIB2 and mAb13), and total (K20) β1 integrin, including self-colocalization controls. By showing representative STED images of all ab colocalizations, this panel complements the Fig. 3 E. Also within Fig. S2, the lack of competition between the selected abs after fixation is shown as a control. Fig. S3 represents the individual channels of the merged STED images displayed in Fig. 4 for better clarity.

Acknowledgments

We acknowledge grants to S. Strömblad and M. Lakadamyali from the European Union 7th Framework Programme Systems Microscopy Network of Excellence (grant HEALTH-F4-2010-258068), to S. Strömblad from the Swedish Research Council (grants 340-2012-6001 and 521-2012-3180), the Swedish Strategic Research Foundation, and the Swedish Cancer Society, and to M. Lakadamyali from the Fundación Cellex, Barcelona, European Union 7th Framework Programme European Research Council 337191-MOTORS, the Spanish Ministry of Economy and Competitiveness, the European Regional Development Fund grant FIS2015-63550-R (Ministry of Economy and Competitiveness/Fondo Europeo de Desarollo Regional) and the Ministry of Economy and Competitiveness Severo Ochoa program for Centers of Excellence in Research and Development (SEV-2015-0522). P. Hernandez-Varas was partially funded by the Ramón Areces Foundation and by the Wolfson Imaging Centre at the University of Oxford, where part of the STED imaging was performed. STED and confocal imaging was also carried out at the Advanced Light Microscopy facility at Science for Life Laboratory. STORM imaging was in part carried out at the Nikon Cluster of Excellence in STORM at the Institute of Photonic Sciences. Confocal, TIRF, and part of the STORM microscopy imaging occurred at the live-cell imaging facility and Nikon Cluster of Excellence at Karolinska Institutet, supported by grants from the Knut and Alice Wallenberg Foundation, the Swedish Research Council, the Centre for Innovative Medicine, the Jonasson Donation to the Royal Institute of Technology, and a Karolinska Institutet core facility grant. The funders had no role in study design, data collection and analysis, decision to publish, or preparation of the manuscript.

The authors declare no competing financial interests.

Author contributions: M. Spiess, P. Hernandez-Varas, J.G. Lock, and S. Strömblad designed research. M. Spiess, P. Hernandez-Varas, A. Oddone, H. Olofsson, and H. Blom performed experiments. M. Spiess, P. Hernandez-Varas, A. Oddone, and D. Waithe analyzed data. M. Lakadamyali and S. Strömblad supervised research. M. Spiess and S. Strömblad drafted the paper. All authors contributed to the edit.

Submitted: 13 July 2017
Revised: 16 February 2018
Accepted: 26 March 2018

References

Akiyama, S.K., S.S. Yamada, W.T. Chen, and K.M. Yamada. 1989. Analysis of fibronectin receptor function with monoclonal antibodies: roles in cell adhesion, migration, matrix assembly, and cytoskeletal organization. *J. Cell Biol.* 109:863–875. https://doi.org/10.1083/jcb.109.2.863

Amiot, M., A. Bernard, H.C. Tran, G. Leca, J.M. Kanellopoulos, and L. Boumsell. 1986. The human cell surface glycoprotein complex (gp 120,200) recognized by monoclonal antibody K20 is a component binding to phytohaemagglutinin on T cells. *Scand. J. Immunol.* 23:109–118. https://doi.org/10.1111/j.1365-3083.1986.tb01948.x

Bates, M., B. Huang, G.T. Dempsey, and X. Zhuang. 2007. Multicolor super-resolution imaging with photo-switchable fluorescent probes. *Science.* 317:1749–1753. https://doi.org/10.1126/science.1146598

Bazzoni, G., D.T. Shih, C.A. Buck, and M.E. Hemler. 1995. Monoclonal antibody 9EG7 defines a novel beta 1 integrin epitope induced by soluble ligand and manganese, but inhibited by calcium. *J. Biol. Chem.* 270:25570–25577. https://doi.org/10.1074/jbc.270.43.25570

Blom, H., and J. Widengren. 2017. Stimulated Emission Depletion Microscopy. *Chem. Rev.* 117:7377–7427. https://doi.org/10.1021/acs.chemrev.6b00653

Bouvard, D., J. Pouwels, N. De Franceschi, and J. Ivaska. 2013. Integrin inactivators: balancing cellular functions in vitro and in vivo. *Nat. Rev. Mol. Cell Biol.* 14:430–442. https://doi.org/10.1038/nrm3599

Burridge, K., and C. Guilluy. 2016. Focal adhesions, stress fibers and mechanical tension. *Exp. Cell Res.* 343:14–20. https://doi.org/10.1016/j.yexcr.2015.10.029

Byron, A., J.D. Humphries, J.A. Askari, S.E. Craig, A.P. Mould, and M.J. Humphries. 2009. Anti-integrin monoclonal antibodies. *J. Cell Sci.* 122:4009–4011. https://doi.org/10.1242/jcs.056770

Campbell, I.D., and M.J. Humphries. 2011. Integrin structure, activation, and interactions. *Cold Spring Harb. Perspect. Biol.* 3:a004994. https://doi.org/10.1101/cshperspect.a004994

Changede, R., and M. Sheetz. 2017. Integrin and cadherin clusters: A robust way to organize adhesions for cell mechanics. *BioEssays.* 39:1–12. https://doi.org/10.1002/bies.201600123

Dempsey, G.T., J.C. Vaughan, K.H. Chen, M. Bates, and X. Zhuang. 2011. Evaluation of fluorophores for optimal performance in localization-based super-resolution imaging. *Nat. Methods.* 8:1027–1036. https://doi.org/10.1038/nmeth.1768

Deschout, H., A. Shivanandan, P. Annibale, M. Scarselli, and A. Radenovic. 2014. Progress in quantitative single-molecule localization microscopy. *Histochem. Cell Biol.* 142:5–17. https://doi.org/10.1007/s00418-014-1217-y

Diez-Ahedo, R., D. Normanno, O. Esteban, G.J. Bakker, C.G. Figdor, A. Cambi, and M.F. Garcia-Parajo. 2009. Dynamic re-organization of individual adhesion nanoclusters in living cells by ligand-patterned surfaces. *Small.* 5:1258–1263. https://doi.org/10.1002/smll.200801699

Dunn, K.W., M.M. Kamocka, and J.H. McDonald. 2011. A practical guide to evaluating colocalization in biological microscopy. *Am. J. Physiol. Cell Physiol.* 300:C723–C742. https://doi.org/10.1152/ajpcell.00462.2010

Ester, M., H. Kriegel, J. Sander, and X. Xu. 1996. A density based algorithm for discovering clusters in large spatial databases with noise. *Proceedings of the Second International Conference on Knowledge Discovery and Data Mining*:226–231.

Fischler, A.M., and R.C. Bolles. 1981. Random sample consensus: a paradigm for model fitting with applications to image analysis and automated cartography. *Commun. ACM.* 24:381–395. https://doi.org/10.1145/358669.358692

Fornasiero, E.F., and F. Opazo. 2015. Super-resolution imaging for cell biologists: concepts, applications, current challenges and developments. *BioEssays.* 37:436–451. https://doi.org/10.1002/bies.201400170

French, J.B., S.A. Jones, H. Deng, A.M. Pedley, D. Kim, C.Y. Chan, H. Hu, R.J. Pugh, H. Zhao, Y. Zhang, et al. 2016. Spatial colocalization and functional link of purinosomes with mitochondria. *Science.* 351:733–737. https://doi.org/10.1126/science.aac6054

Geiger, B., and K.M. Yamada. 2011. Molecular architecture and function of matrix adhesions. *Cold Spring Harb. Perspect. Biol.* 3:a005033. https://doi.org/10.1101/cshperspect.a005033

Goyette, J., and K. Gaus. 2017. Mechanisms of protein nanoscale clustering. *Curr. Opin. Cell Biol.* 44:86–92. https://doi.org/10.1016/j.ceb.2016.09.004

Han, M.K., and J. de Rooij. 2016. Converging and Unique Mechanisms of Mechanotransduction at Adhesion Sites. *Trends Cell Biol.* 26:612–623. https://doi.org/10.1016/j.tcb.2016.03.005

Hantgan, R.R., M. Rocco, C. Nagaswami, and J.W. Weisel. 2001. Binding of a fibrinogen mimetic stabilizes integrin alphaIIbbeta3's open conformation. *Protein Sci.* 10:1614–1626. https://doi.org/10.1110/ps.3001

Hoffmann, J.E., Y. Fermin, R.L. Stricker, K. Ickstadt, and E. Zamir. 2014. Symmetric exchange of multi-protein building blocks between stationary focal adhesions and the cytosol. *eLife.* 3:e02257. https://doi.org/10.7554/eLife.02257

Horton, E.R., A. Byron, J.A. Askari, D.H.J. Ng, A. Millon-Frémillon, J. Robertson, E.J. Koper, N.R. Paul, S. Warwood, D. Knight, et al. 2015. Definition of a consensus integrin adhesome and its dynamics during adhesion complex assembly and disassembly. *Nat. Cell Biol.* 17:1577–1587. https://doi.org/10.1038/ncb3257

Hu, S., Y.H. Tee, A. Kabla, R. Zaidel-Bar, A. Bershadsky, and P. Hersen. 2015. Structured illumination microscopy reveals focal adhesions are composed of linear subunits. *Cytoskeleton (Hoboken).* 72:235–245. https://doi.org/10.1002/cm.21223

Hynes, R.O. 2002. Integrins: bidirectional, allosteric signaling machines. *Cell.* 110:673–687. https://doi.org/10.1016/S0092-8674(02)00971-6

Hynes, R.O., and A. Naba. 2012. Overview of the matrisome--an inventory of extracellular matrix constituents and functions. *Cold Spring Harb. Perspect. Biol.* 4:a004903. https://doi.org/10.1101/cshperspect.a004903

Kanchanawong, P., G. Shtengel, A.M. Pasapera, E.B. Ramko, M.W. Davidson, H.F. Hess, and C.M. Waterman. 2010. Nanoscale architecture of integrin-based cell adhesions. *Nature.* 468:580–584. https://doi.org/10.1038/nature09621

Klar, T.A., and S.W. Hell. 1999. Subdiffraction resolution in far-field fluorescence microscopy. *Opt. Lett.* 24:954–956. https://doi.org/10.1364/OL.24.000954

Köhler, K., S. Xiong, J. Brzostek, M. Mehrabi, P. Eissmann, A. Harrison, S.P. Cordoba, S. Oddos, V. Miloserdov, K. Gould, et al. 2010. Matched sizes of activating and inhibitory receptor/ligand pairs are required for optimal signal integration by human natural killer cells. *PLoS One.* 5:e15374. https://doi.org/10.1371/journal.pone.0015374

Lenter, M., H. Uhlig, A. Hamann, P. Jenö, B. Imhof, and D. Vestweber. 1993. A monoclonal antibody against an activation epitope on mouse integrin chain beta 1 blocks adhesion of lymphocytes to the endothelial integrin alpha 6 beta 1. *Proc. Natl. Acad. Sci. USA.* 90:9051–9055. https://doi.org/10.1073/pnas.90.19.9051

Le Saux, G., A. Magenau, K. Gunaratnam, K.A. Kilian, T. Böcking, J.J. Gooding, and K. Gaus. 2011. Spacing of integrin ligands influences signal transduction in endothelial cells. *Biophys. J.* 101:764–773. https://doi.org/10.1016/j.bpj.2011.06.064

Li, J., Y. Su, W. Xia, Y. Qin, M.J. Humphries, D. Vestweber, C. Cabañas, C. Lu, and T.A. Springer. 2017. Conformational equilibria and intrinsic affinities define integrin activation. *EMBO J.* 36:629–645. https://doi.org/10.15252/embj.201695803

Lock, J.G., B. Wehrle-Haller, and S. Strömblad. 2008. Cell-matrix adhesion complexes: master control machinery of cell migration. *Semin. Cancer Biol.* 18:65–76. https://doi.org/10.1016/j.semcancer.2007.10.001

Luque, A., M. Gómez, W. Puzon, Y. Takada, F. Sánchez-Madrid, and C. Cabañas. 1996. Activated conformations of very late activation integrins detected by a group of antibodies (HUTS) specific for a novel regulatory region (355-425) of the common beta 1 chain. *J. Biol. Chem.* 271:11067–11075. https://doi.org/10.1074/jbc.271.19.11067

Moser, M., K.R. Legate, R. Zent, and R. Fässler. 2009. The tail of integrins, talin, and kindlins. *Science.* 324:895–899. https://doi.org/10.1126/science.1163865

Mould, A.P., A.N. Garratt, J.A. Askari, S.K. Akiyama, and M.J. Humphries. 1995. Identification of a novel anti-integrin monoclonal antibody that

recognises a ligand-induced binding site epitope on the beta 1 subunit. *FEBS Lett.* 363:118–122. https://doi.org/10.1016/0014-5793(95)00301-O

Mould, A.P., S.K. Akiyama, and M.J. Humphries. 1996. The inhibitory anti-beta1 integrin monoclonal antibody 13 recognizes an epitope that is attenuated by ligand occupancy. Evidence for allosteric inhibition of integrin function. *J. Biol. Chem.* 271:20365–20374. https://doi.org/10.1074/jbc.271.34.20365

Nan, X., E.A. Collisson, S. Lewis, J. Huang, T.M. Tamgüney, J.T. Liphardt, F. McCormick, J.W. Gray, and S. Chu. 2013. Single-molecule superresolution imaging allows quantitative analysis of RAF multimer formation and signaling. *Proc. Natl. Acad. Sci. USA.* 110:18519–18524. https://doi.org/10.1073/pnas.1318188110

Neumann, D., J. Bückers, L. Kastrup, S.W. Hell, and S. Jakobs. 2010. Two-color STED microscopy reveals different degrees of colocalization between hexokinase-I and the three human VDAC isoforms. *PMC Biophys.* 3:4. https://doi.org/10.1186/1757-5036-3-4

Park, C.C., H.J. Zhang, E.S. Yao, C.J. Park, and M.J. Bissell. 2008. Beta1 integrin inhibition dramatically enhances radiotherapy efficacy in human breast cancer xenografts. *Cancer Res.* 68:4398–4405. https://doi.org/10.1158/0008-5472.CAN-07-6390

Paszek, M.J., C.C. DuFort, O. Rossier, R. Bainer, J.K. Mouw, K. Godula, J.E. Hudak, J.N. Lakins, A.C. Wijekoon, L. Cassereau, et al. 2014. The cancer glycocalyx mechanically primes integrin-mediated growth and survival. *Nature.* 511:319–325. https://doi.org/10.1038/nature13535

Patla, I., T. Volberg, N. Elad, V. Hirschfeld-Warneken, C. Grashoff, R. Fässler, J.P. Spatz, B. Geiger, and O. Medalia. 2010. Dissecting the molecular architecture of integrin adhesion sites by cryo-electron tomography. *Nat. Cell Biol.* 12:909–915. https://doi.org/10.1038/ncb2095

Roca-Cusachs, P., N.C. Gauthier, A. Del Rio, and M.P. Sheetz. 2009. Clustering of $\alpha_5\beta_1$ integrins determines adhesion strength whereas $\alpha_v\beta_3$ and talin enable mechanotransduction. *Proc. Natl. Acad. Sci. USA.* 106:16245–16250. https://doi.org/10.1073/pnas.0902818106

Rossier, O., and G. Giannone. 2016. The journey of integrins and partners in a complex interactions landscape studied by super-resolution microscopy and single protein tracking. *Exp. Cell Res.* 343:28–34. https://doi.org/10.1016/j.yexcr.2015.11.004

Rossier, O., V. Octeau, J.B. Sibarita, C. Leduc, B. Tessier, D. Nair, V. Gatterdam, O. Destaing, C. Albigès-Rizo, R. Tampé, et al. 2012. Integrins β1 and β3 exhibit distinct dynamic nanoscale organizations inside focal adhesions. *Nat. Cell Biol.* 14:1057–1067. https://doi.org/10.1038/ncb2588

Rust, M.J., M. Bates, and X. Zhuang. 2006. Sub-diffraction-limit imaging by stochastic optical reconstruction microscopy (STORM). *Nat. Methods.* 3:793–796. https://doi.org/10.1038/nmeth929

Schmied, J.J., A. Gietl, P. Holzmeister, C. Forthmann, C. Steinhauer, T. Dammeyer, and P. Tinnefeld. 2012. Fluorescence and super-resolution standards based on DNA origami. *Nat. Methods.* 9:1133–1134. https://doi.org/10.1038/nmeth.2254

Schoonderwoert, V., R. Dijkstra, G. Luckinavicius, O. Kobler, and H. Van Der Voort. 2013. Huygens STED deconvolution increases signal-to-noise and image resolution towards 22 nm. *Micros. Today.* 21:38–44. https://doi.org/10.1017/S1551929513001089

Shibata, A.C., T.K. Fujiwara, L. Chen, K.G. Suzuki, Y. Ishikawa, Y.L. Nemoto, Y. Miwa, Z. Kalay, R. Chadda, K. Naruse, and A. Kusumi. 2012. Archipelago architecture of the focal adhesion: membrane molecules freely enter and exit from the focal adhesion zone. *Cytoskeleton (Hoboken).* 69:380–392. https://doi.org/10.1002/cm.21032

Shivanandan, A., H. Deschout, M. Scarselli, and A. Radenovic. 2014. Challenges in quantitative single molecule localization microscopy. *FEBS Lett.* 588:3595–3602. https://doi.org/10.1016/j.febslet.2014.06.014

Shroff, H., C.G. Galbraith, J.A. Galbraith, H. White, J. Gillette, S. Olenych, M.W. Davidson, and E. Betzig. 2007. Dual-color superresolution imaging of genetically expressed probes within individual adhesion complexes. *Proc. Natl. Acad. Sci. USA.* 104:20308–20313. https://doi.org/10.1073/pnas.0710517105

Sidenstein, S.C., E. D'Este, M.J. Böhm, J.G. Danzl, V.N. Belov, and S.W. Hell. 2016. Multicolour Multilevel STED nanoscopy of Actin/Spectrin Organization at Synapses. *Sci. Rep.* 6:26725. https://doi.org/10.1038/srep26725

Singh, P., C. Carraher, and J.E. Schwarzbauer. 2010. Assembly of fibronectin extracellular matrix. *Annu. Rev. Cell Dev. Biol.* 26:397–419. https://doi.org/10.1146/annurev-cellbio-100109-104020

Snapp, E. 2005. Design and use of fluorescent fusion proteins in cell biology. *Curr. Protoc. Cell Biol.* 21:24.

Su, Y., W. Xia, J. Li, T. Walz, M.J. Humphries, D. Vestweber, C. Cabañas, C. Lu, and T.A. Springer. 2016. Relating conformation to function in integrin α5β1. *Proc. Natl. Acad. Sci. USA.* 113:E3872–E3881. https://doi.org/10.1073/pnas.1605074113

Takada, Y., and W. Puzon. 1993. Identification of a regulatory region of integrin beta 1 subunit using activating and inhibiting antibodies. *J. Biol. Chem.* 268:17597–17601.

Tam, J., and D. Merino. 2015. Stochastic optical reconstruction microscopy (STORM) in comparison with stimulated emission depletion (STED) and other imaging methods. *J. Neurochem.* 135:643–658. https://doi.org/10.1111/jnc.13257

Werb, Z., P.M. Tremble, O. Behrendtsen, E. Crowley, and C.H. Damsky. 1989. Signal transduction through the fibronectin receptor induces collagenase and stromelysin gene expression. *J. Cell Biol.* 109:877–889. https://doi.org/10.1083/jcb.109.2.877

Xu, L., D. Rönnlund, P. Aspenström, L.J. Braun, A.K. Gad, and J. Widengren. 2016. Resolution, target density and labeling effects in colocalization studies - suppression of false positives by nanoscopy and modified algorithms. *FEBS J.* 283:882–898. https://doi.org/10.1111/febs.13652

Zhu, J., B.H. Luo, T. Xiao, C. Zhang, N. Nishida, and T.A. Springer. 2008. Structure of a complete integrin ectodomain in a physiologic resting state and activation and deactivation by applied forces. *Mol. Cell.* 32:849–861. https://doi.org/10.1016/j.molcel.2008.11.018

Zhu, J., J. Zhu, and T.A. Springer. 2013. Complete integrin headpiece opening in eight steps. *J. Cell Biol.* 201:1053–1068. https://doi.org/10.1083/jcb.201212037